# Comparative Design of Ferrite- and NdFeB-PMSMs using the (x,b) Design Plane



(Article begins on next page)

# Comparative Design of Ferrite- and NdFeB-PMSMs using the (x,b) Design Plane

Gaetano Dilevrano
*Dipartimento Energia Galileo Ferraris*
*Politecnico di Torino*
Turin, Italy
gaetano.dilevrano@polito.it

Paolo Ragazzo
*Dipartimento Energia Galileo Ferraris*
*Politecnico di Torino*
Turin, Italy
paolo.ragazzo@polito.it

Simone Ferrari
*Dipartimento Energia Galileo Ferraris*
*Politecnico di Torino*
Turin, Italy
simone.ferrari@polito.it

Gianmario Pellegrino
*Dipartimento Energia Galileo Ferraris*
*Politecnico di Torino*
Turin, Italy
gianmario.pellegrino@polito.it

***Abstract*—In this paper, two permanent magnet synchronous motors for traction application are designed and compared using the open-source design platform SyR-e, the first one using NdFeB magnets and the second ferrite magnets, as a rare-earth free alternative. The core of the adopted design method is the $(x, b)$ plane, where a number of performance indicators are shown function of the two geometric parameters $x$ and $b$ of the machine cross-section. Performance figures are calculated using approximated design equations, corrected with the fast finite-element analysis FEAfix approach, to obtain FEA-like accuracy with a limited computational effort. New figures of merit have been added to the plane to visually match the output figures and the design constraints. Special attention is devoted in this paper to the ferrite-magnet motor and its demagnetization limit. Because of the low energy density and coercivity of ferrite magnets, this motor will need an increased stack length and inverter current rating. Besides the direct comparison of the two motors throughout the design and FEA identification steps, the paper also gives a complete overview of how SyR-e is used for fast preliminary motor design starting from design specs and target figures.**

***Index Terms*—*Open-source software, Open Science, AC motors Design, Electric Motor Design, E-Axle, Finite Element Analysis, Interior PM motors, Permanent Magnet Synchronous Motors***

## I. Introduction

Today, electrified axles for traction applications see the widespread use of permanent magnet synchronous machines (PMSM) with NdFeB magnets [1] [2]. At the same time, the scarcity and price instability of rare-earth materials [3] are pushing the automotive industry towards alternative solutions [4]. Among these, the PM-assisted synchronous reluctance (PM-SyR) machine with ferrite PMs is considered a promising rare-earth free alternative, as already done in hybrid-electric drivetrains as far as in 2016 [5]. This paper proposes a full design procedure for the design of PMSMs for traction applications, comparing an Interior Permanent Magnet (IPM) motor with NdFeB PMs and a ferrite PM-SyR motor. The critical aspects of IPM and PM-SyR motors, like short-circuit

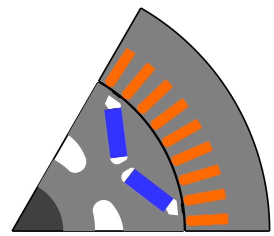

Fig. 1. Cross-section of the benchmark, inspired by the Tesla Model 3 3D6.

TABLE I
Tesla Model 3 3D6 specs and dimensions [8].

| | | | |
|---|---|---|---|
| Peak torque | $T_{max}$ | 440 | [Nm] |
| Peak power | $P_{max}$ | 220 | [kW] |
| Maximum speed | $n_{max}$ | 18100 | [rpm] |
| DC link voltage | $V_{dc}$ | 320 | [V] |
| Peak phase current | $I_{max}$ | 1131 | [A] |
| Stator outer diameter | $D$ | 225 | [mm] |
| Stack length | $L$ | 114 | [mm] |
| Airgap length | $g$ | 0.7 | [mm] |
| Number of pole pairs | $p$ | 3 | |
| Number of slot/pole/phase | $q$ | 3 | |

currents and irreversible PM demagnetization are considered during the preliminary design, improving the design procedure presented in [6] with new performance figures, and giving more insights on the $(x, b)$ design plane approach implemented in the open-source environment SyR-e [7].

SyR-e stands for Synchronous Reluctance Evolution and is a Matlab-based environment available on GitHub for the design and simulation of electrical machines and drives [7]. SyR-e covers different kinds of AC motors such as synchronous reluctance and permanent magnet machines with different stator and rotor typologies. Moreover, SyR-e is directly interfaced with the magnetostatic FEA client FEMM [9] for freeware FEA simulations. The software is developed for targeting all-level designers via two main graphical user interfaces (GUIs): the first focuses on the design, simulation and optimization of the machine, while the second is for control trajectories evaluation, efficiency maps computation [10], fast scaling and skewing evaluation, and creation of the 1D dynamic model for control development purposes [11]. Besides the design optimization and evaluation of the performance figures of an existing motor, one of the most important features of SyR-e is the preliminary design procedure based on the FEAfix corrected $(x, b)$ design plane, allowing a quick convergence to a good preliminary design, starting from the targets and requirements of the application. A new third GUI is introduced, dedicated to the manipulation of the design plane, included in the last release of SyR-e. Note that all the material presented in the paper is available in form of ready-to-use Matlab scripts that can be freely developed by any user, under the generous conditions of the Apache 2.0 licence [12].

In the following, two traction motors will be designed and compared. They are based on the specifications of the Tesla Model 3 3D6 motor [8] reported in Table I, while its cross-section is displayed in Fig.1. The first design is an IPM motor with NdFeB PMs in a double-V arrangement, while the second is a PM-SyR motor with ferrite PMs, with a 3-layers rotor with circular-barriers. Special care will be devoted to the early determination of the demagnetization limit, of particular importance for the ferrite PM machine. In section II the $(x, b)$ design plane is reviewed and new indicators are introduced. Section III shows the design planes of the IPM and PM-SyR motors, together with the iterative strategy used to meet the target performance figures. Finally, the performance and limits of the two machines are compared in section IV.

## II. THE $(x, b)$ DESIGN PLANE

The $(x, b)$ design plane allows the fast parametric design and evaluation of SyR and PMSM machines [6], [13]. Given the outer dimensions of the motor stack (outer diameter $D$ and length $L$), the allowed current density $J(\mathrm{A/mm^2})$ and peak flux density $B_{Fe}(\mathrm{T})$, the design plane organizes the machine cross-section according to the rotor split ratio $x$ and the iron/air split ratio $b$ coordinates:

$$x = \frac{D_r}{D} \qquad b = \frac{B_g}{B_{Fe,s}} \tag{1}$$

where $D_r$ is the rotor diameter, $B_g$ the airgap peak flux density and $B_{Fe,s}$ is the stator back iron peak flux density. These definitions assume a sinusoidal flux density distribution at the airgap.

### A. Design Equations

Approximated design equations are adopted in the first instance to estimate the motor figures of merit. The flux equations of a PMSM are reported in (2), normalized by the number of turns in series per phase $N_s$.

$$\begin{cases} \lambda_d/N_s = (L_{md} + L_\sigma)/N_s^2 \cdot (N_s i_d) + \lambda_m/N_s \\ \lambda_q/N_s = (L_{mq} + L_\sigma)/N_s^2 \cdot (N_s i_q) \end{cases} \tag{2}$$

The four parameters $L_{md}$, $L_{mq}$, $L_\sigma$ and $\lambda_m$ are the magnetizing inductance of the $d$ and $q$ axes, the leakage inductance and the PM flux linkage, respectively, and they are analytically evaluated as explained in [13] and [6]. The normalization by $N_s$ tells that the design plane shows the Ampere-turn function of $(x, b)$ given the peak current density $J$ and the Volt-second per turn function of $(x, b)$ given the peak flux density $B_{Fe}$ and not yet the respective quantities at the machine terminals. The terms $L_d$ and $L_q$ are defined as the sum of the respective magnetizing and leakage inductance.

Performance figures are summarized by torque $T$ and power factor $cos(\varphi)$ defined as:

$$T = \frac{3}{2} p \cdot (\lambda_d \cdot i_q - \lambda_q \cdot i_d) \tag{3}$$

$$cos\varphi = sin(\gamma - \delta) \tag{4}$$

Where $p$ is the number of pole pairs, $\gamma$ and $\delta$ are current and flux linkage phase angles with respect to the $d$-axis, related to the same parameters of the model evaluated for torque. The resistance voltage is neglected in (4) On the plane, torque and power factor are considered at maximum torque per ampere (MTPA) conditions, and depend on the cross-section geometry summarized by $D$ and the two coordinates $x$ and $b$, on the stack length $L$, and on the peak current density and flux density. From (2) and (3) it can be noticed that $T$ at given geometry and peak $J$ and $B_{Fe}$ is independent of the number of turns $N_s$. This is functional to the proposed design procedure as said, and allows the selection and optimization of $N_s$ at the end of the design process.

### B. Characteristic current computation

A novel contribution of the paper is the early computation of the motor characteristic current $I_{ch}$ on the design plane. $I_{ch}$ is defined as in (5) and is an indicator of the flux weakening capability of the machine.

$$I_{ch} = \frac{\lambda_m}{L_d} \tag{5}$$

The design plane will report the $N_s \cdot I_{ch}$ curves following the definition (5) and the method presented later for correcting the approximated parameters $\lambda_m$ and $L_d$.

### C. Peak short circuit current computation

Another new feature of the design plane is the estimate of the peak transient short circuit current (Ampere-turns) curves. The Hyper Worst Case (HWC) short-circuit current $I_{HWC}$ defined in [14] corresponds to the peak short circuit current in a lossless machine and will be adopted in the following. For the same machine, the HWC current depends on the pre-fault operating point; in particular, the worst pre-fault operating point corresponds to maximum torque and maximum flux linkage $\lambda_{max}$. The equation defining $I_{HWC}$ follows, from the magnetic parameters of the motor (6).

$$\lambda_d(i_d = I_{HWC}, i_q = 0) = -\lambda_{max} \tag{6}$$

As for the characteristic current, this equation will be FEA corrected as presented later.

### D. FEAfix refinement

The analytical model inaccuracy is related to iron saturation and $dq$ cross-saturation. The FEAfix calibration approach consists of applying corrective factors over the $(x, b)$ plane computed by few selected FEA simulations. In the following, 16 points (16 design cross-sections) over a 4x4 regular grid are selected as FEA-computed designs whose parameters are considered exact: the correction factors are evaluated at the points of the grid and then extended over the design plane with bi-linear interpolation. The FEAfix cases are parallel-computed to reduce computational time. For each considered FEAfix cross-section, the MTPA current $\gamma$ angle is found iteratively. The correction factors are defined as:

$$\begin{cases} k_d = \frac{\lambda_d^{FEA}(i_d,i_q) - \lambda_d^{FEA}(0,0)}{\lambda_d^{model} - \lambda_m^{model}} \\ k_q = \frac{\lambda_q^{FEA}(i_d,i_q)}{\lambda_q^{model}} \\ k_m = \frac{\lambda_d^{FEA}(0,0)}{\lambda_m^{model}} \\ k_{ch} = \frac{i_{ch}^{FEA}}{i_{ch}^{model}} \\ k_{HWC} = \frac{i_{HWC}^{FEA}}{i_{HWC}^{model}} \end{cases} \tag{7}$$

Here the superscript $FEA$ identifies the results of the FEA simulations, while the superscript $model$ the results of the analytical model behind the design plane. The correction factors are $k_d$ for $d$-axis flux linkage (armature contribution), $k_q$ for the $q$-axis flux linkage, $k_m$ for the PM flux linkage, $k_{ch}$ for the characteristic current and $k_{HWC}$ for the HWC short-circuit current. The first three factors are computed by iterative search of the MTPA point $(i_d, i_q)$ plus one open-circuit simulation. The FEA research of $I_{ch}$ requires also iterations: the zero current simulation used for the PM flux linkage and $k_m$ is used as the starting point, while following simulations impose increasing currents aiming to obtain null flux linkage along the PM axis. A similar method is adopted to FEA-compute the correct HWC current. As explained in [14], an iterative secant method is exploited to solve (6). Then, the factor $k_{HWC}$ is computed using this FEA-evaluated HWC current.

The baseline version on the design plane is reported in Fig. 2. Here, the two main performance figures (torque and power factor) are reported as contours over the $(x, b)$ domain. The green points represent the 16 motors at the base of the FEAfix procedure. There, the correction factors are computed with FEA and then extended to the full design plane by means of bilinear interpolation.

The plot in Fig. 2 is the standard form of the design plane plotted by SyR-e. Besides it shows just torque and power factor contours, other information is stored in the figure, enabling

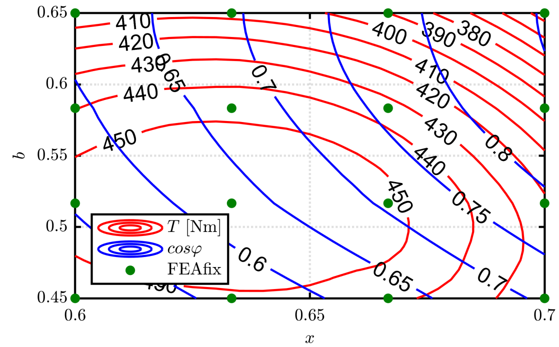


Fig. 2. Example of $(x, b)$ design plane: torque and power factor reported function of $(x, b)$ with red and blue contours respectively. FEAfix points are marked with green dots.

several considerations and elaborations in post-processing that are at the base of the design procedure. For instance, the current components, flux linkages and FEAfix factors are stored, as well as all the other figures introduced in this paper. Furthermore, it is possible to instantaneously:

- performs axial scaling as reported in [15];
- compute the performance at different numbers of turns in series per phase $N_s$.

### E. Demagnetization analysis

In the design plane, demagnetization is early verified at the two reference current levels:

- $I_{max}$ at MTPA, to ensure that the motor can work at peak torque conditions;
- $I_{HWC}$, referring to short circuit conditions (ACS or fault).

For each FEAfix design, one dedicated FEA simulation is performed per current value, and the flux density at each mesh element of the PMs is saved. If the flux density is lower than the knee point of the BH curve of the material, the node is identified as demagnetized. The result of the simulation is the percentage of demagnetized PM volume. Once again, the demagnetization index computed for the 16 FEAfix designs is then extended over the $(x, b)$ plane via interpolation.

### F. Manipulation of the design plane results

Once the design plane is evaluated, its data can be elaborated to easily select the best machine for the proposed application. The power factor specification is computed from the specified peak power request and maximum current. First, the (minimum) base speed, required to fulfil both $T$ and $P$ targets is:

$$n_{base} = \frac{30}{\pi} \cdot \frac{P_{max}}{T_{max}} \tag{8}$$

corresponding to $n_{base} \geq 4775$ rpm for the selected design. Then, the maximum power is associated with this speed value as:

$$P_{max} = \frac{\sqrt{3}}{2} \cdot V_{dc} \cdot I_{max} \cdot cos\varphi_{base} \cdot \eta \tag{9}$$

where $\eta$ is the efficiency (unknown at this stage). The target power factor is computed as:

$$cos\varphi_{base} \geq \frac{2}{\sqrt{3}} \frac{P_{max}}{V_{dc} \cdot I_{max} \cdot \eta} \tag{10}$$

Assuming a unitary efficiency, the target power factor related to the data reported in Table I is around 0.7. For a lower efficiency, a slightly higher target power factor is required.

The peak torque and power requirements are summarized in the torque and power factor constraints of (11):

$$\begin{cases} T(x,b) \geq T_{max} \\ cos\varphi(x,b) \geq cos\varphi_{base} \end{cases} \tag{11}$$

that will define two corresponding areas of feasibility in the $(x,b)$ domain.

### G. Number of turns selection

A key step in the selection of a candidate design from the $(x,b)$ plane is the determination of feasible numbers of turns. This choice must account for the inverter limits, the performance figures (reported on the design plane) and the geometric constraints of the motor. If hairpin windings are considered, as for the benchmark, the feasible number of turns is even more constrained, impeding the fine-tuning of this parameter: the number of conductors per slot is limited to an even number, lower than 10, with rigid constraints on the number of parallels [16], [17].

For the $N_s$ selection, two quantities are of interest: the ampere-turns contours $N_s \cdot I$ and the flux contours $\frac{\lambda}{N_s}$. These are directly computed from the input current density of the design plane $J$ and the motor geometry. The two quantities are fundamental to account for the current and voltage constraints. To fulfill the current constraint, the design current (computed from $J$ input) must be lower or equal to the inverter limit. Including the number of turns, this constraint becomes:

$$N_s \cdot I(x,b) \leq N_s^* \cdot I_{max} \tag{12}$$

where $N_s^*$ is an imposed and feasible number of turns. Dealing with voltage, the process is slightly more complex. The compliance with the voltage limit is expressed as:

$$V_{dc} = n_{base} \cdot p \cdot \frac{\pi}{30} \cdot \lambda_{max} \tag{13}$$

where $p$ is the number of pole pairs and $\lambda_{max}$ is the peak flux linkage, usually reached in peak torque condition at base speed (that is the operating point evaluated on the design plane). This equation translates the inverter voltage constraint into a flux linkage limit, given that the base speed requirement (8) is fulfilled. Imposing a feasible number of turns $N_s^*$, the voltage constraint becomes:

$$\frac{\lambda}{N_s}(x,b) \leq \frac{\lambda_{max}}{N_s^*} = \frac{V_{dc}}{p \cdot n_{base} \cdot \frac{\pi}{30} \cdot N_s^*} \tag{14}$$

In the end, it is possible to define, for each feasible number of turns $N_s^*$, a feasibility area on the $(x,b)$ plane, according to (12) and (14), as will be demonstrated later with the case studies.

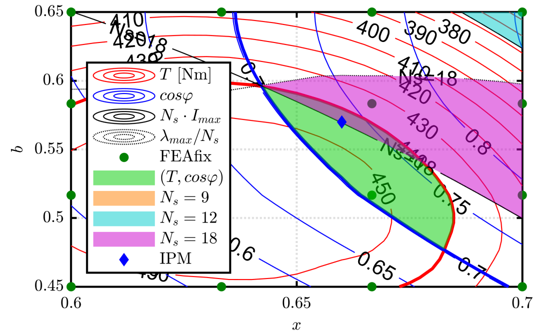


(a)

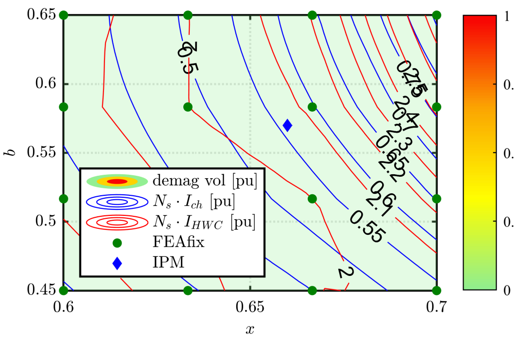


(b)

Fig. 3. Design planes of the IPM motor: (a) $T$, $cos\varphi$ and feasibility areas according (11), (12) and (14); (b) characteristic current, HWC current and demagnetization at rated current.

## III. Case Study

As addressed in the introduction, the design plane is adopted to compare NdFeB IPM motor and ferrite PM-SyR motor at the design stage, targeting the same specifications, listed in Table I. The configuration of the two motors is the same as the baseline design: 3 pole pairs and 54 slots, with hairpin winding. To improve the anisotropy, the IPM rotor is designed with two layers and a V-type geometry, while the PM-SyR rotor will have three circular barriers, with arc PMs. Both designs are based on the same current density requirements of 23 A/mm$^2$, ensuring similar thermal behaviour. Dealing with the feasible number of turns, just three combinations are considered:

- $N_s = 9$ : 4 conductors per slot with 4 parallel paths;
- $N_s = 12$ : 4 conductors per slot with 3 parallel paths;
- $N_s = 18$ : 4 conductors per slot with 2 parallel paths.

### A. NdFeB Motor

The design plane of the IPM motor with NdFeB PMs is shown in Fig. 3a, where the FEA-evaluated machines are marked with a green circle. The plane is computed in hot conditions (80°C), which are the more critical ones for these PMs in terms of demagnetization strength. The figure reports the torque and power factor contours in red and blue, respectively, with the target specification highlighted with a bold line. The feasibility area in terms of $T$ and $cos\varphi$ defined in (11) is highlighted in green. The motors not included in the green area cannot fulfil torque and power specifications for the given dimensions and current density. Dealing with the number of turn selection, it can be noted that $N_s = 12$ and $N_s = 18$ appears on the plane (light blue and purple area), while the $N_s = 9$ solution is not feasible on this plane. However, just the purple area intersects the green feasibility area, so 18 turns are selected for the IPM motor. As addressed in the previous section, it is possible to consider further performance figures before selecting a motor. For instance, Fig. 3b shows the characteristic current and HWC short-circuit current contours, reported in per-unit of the design current (i.e. the one computed from the $J$ input), while the colour map represents the percentage of the PM volume demagnetized at this operating current. For the IPM motor, it is worth noting that no demagnetization happens, so the demagnetization limit does not pose a constraint on the plane. Dealing with the characteristic current, it grows from the bottom left to the top right of the plane, indicating that the high-speed power will be higher in this region. The peak short-circuit current has a similar trend, with values at least double the pre-fault current. In the end, the IPM motor is selected at the point marked with a blue diamond, where the feasibility areas are overlapped. It is placed along the current limit contour, ensuring that the inverter maximum current $I_{max}$ matches with the current imposed from the current density $J$. Furthermore, in this point torque and power factor margin are achieved, with a torque of 444 Nm and a power factor of 0.74. The motor will demagnetize neither in operating condition nor in HWC condition, as reported in Table IV. Dealing with the short-circuit current, the value is slightly higher than twice the pre-fault current, which is the best value achievable in the $(T, cos\varphi, N_s)$ feasibility area.

## B. Ferrite Motor

The design plane of the PM-SyR motor with ferrite PMs is evaluated for the same input of the IPM motor and it is shown in Fig. 4.

The only difference is the PM temperature, that is 20°C for the PM-SyR motor, to contemplate the worst demagnetization case. There are two crucial aspects here. First, there is no combination of $T$ and $cos\varphi$ that fulfill (11), and second, all the motors have PMs completely demagnetized at operating current. To tackle this issue, due to the weaker PMs adopted, there are some strategies to be implemented. First, the input current density $J$ is reduced to 20 Arms/mm2 and the ratio between rotor barrier thickness and rotor carrier thickness is changed, to increase the PM thickness and reduce the demagnetization issue. The design plane is then re-computed with these updated inputs and reported in Fig. 5.

At this point, the demagnetization issue at operating current is solved at least in some areas of the design plane, and the other design target can be considered. As reported in Fig. 5, torque and power factor are still too low, pointing out the need to overcome some of the design limits.

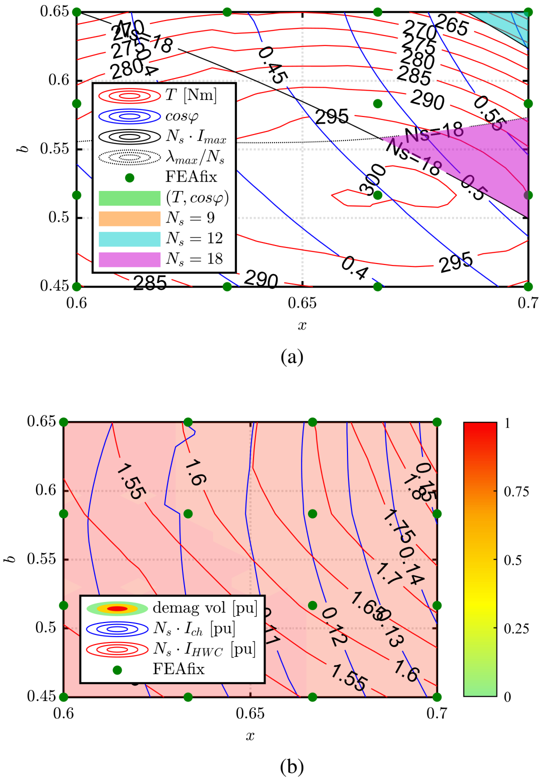


Fig. 4. Design planes of the PM-SyR motor with the same design inputs of IPM motor: (a) $T$, $cos\varphi$ and feasibility areas according (11), (12) and (14); (b) characteristic current, HWC current and demagnetization at rated current.

The $T$ requirement is corrected using the fast axial scaling procedure on the plane. The overlength ratio is roughly computed as the ratio between the target torque and the torque contours in the non-demagnetized area, leading to a stack length of 211 mm. This fulfils the torque specification, but the target power factor must be adjusted too. So, the inverter size is increased, reducing the target power factor (imposed by the power specification). The new maximum current $I_{max}$ is increased to 1100 Arms. The extra-current ratio is roughly computed as the ratio between the target power factor (for the initial inverter limit) and the power factor in the non-demagnetization area of Fig. 5b.

The final PM-SyR design plane is reported in Fig. 6. It is worth noting that the green area in Fig. 6 is visible, while the demagnetization behaviour and the characteristic and HWC current are not changed from the axial scaling. At this point, the PM-SyR motor (marked with a red diamond) is selected close to the torque limit, inside the feasibility area of $N_s = 9$. This selection offers a little margin in current (not exactly coincident with the limit) and a huge margin in terms of power factor and voltage limits. These features will allow the fulfilment of torque specs with no margin or very limited margin and the power spec with a wider margin. Dealing with the demagnetization issue, the motor is safe at the operating current, but not in short-circuit. The characteristic current is around 1/4 of the operating current, meaning that in flux

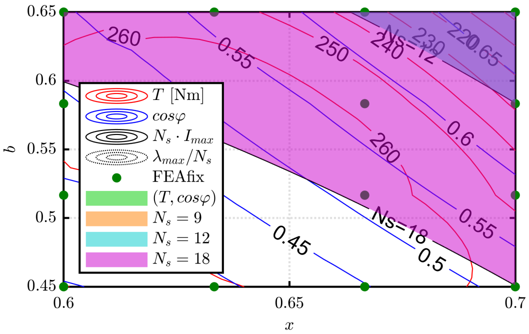


(a)

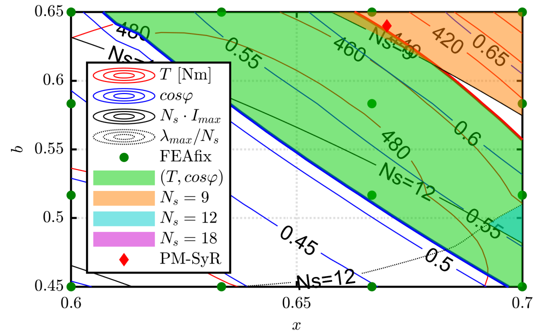


(a)

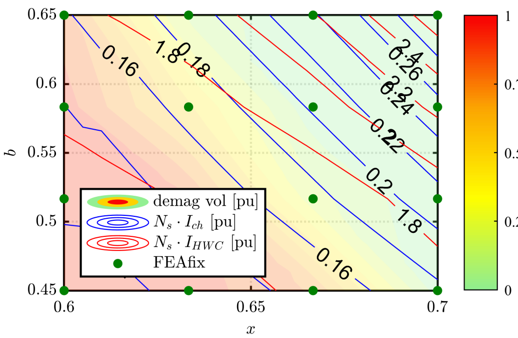


(b)

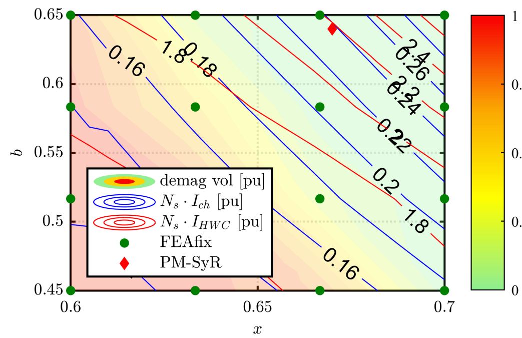


(b)

Fig. 5. Design planes of the PM-SyR motor with reduced current density and thicker PMs: (a) $T$, $cos\varphi$ and feasibility areas according to (11), (12) and (14); (b) characteristic current, HWC current and demagnetization at rated current.

Fig. 6. Design planes of the PM-SyR motor with final stack length and peak current: (a) $T$, $cos\varphi$ and feasibility areas according to (11), (12) and (14); (b) characteristic current, HWC current and demagnetization at rated current.

weakening, the PM-SyR motor will perform worse that the IPM motor (which has a characteristic current of almost half of the design current). The short-circuit overcurrent is similar to the IPM motor, even if the PM contribution is lower, because of the higher anisotropy of the PM-SyR machine.

## IV. Selected Design Comparison

The selected machine cross sections are reported in Fig. 7 and their specification in Tab. IV. The two motors fulfil the torque and power specification, with the difference that the PM-SyR motor is 47% longer than the IPM motor and requires an inverter with a peak current 37.5% higher. The torque versus speed and power versus speed curves are reported in Fig. 8. The blue and red curves represent the IPM and PM-SyR limits, respectively, while the design targets are reported with dashed black lines. The design margin visible on the plane is evident in these two plots. Dealing with the IPM motor, there was a torque margin, visible in Fig. 8a, and a slightly wider power factor margin, that increase the output power of this motor above the design goal. On the contrary, the PM-SyR motor had a slightly lower torque on the design plane, but wide current and power factor margins. The current margin is able to compensate for the torque output, while the power factor margin increases the base speed and the maximum power. Dealing with the power in flux weakening, the IPM motor performs better than the PM-SyR motor, as expected from the

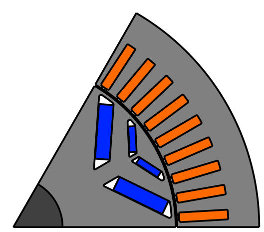

(a)

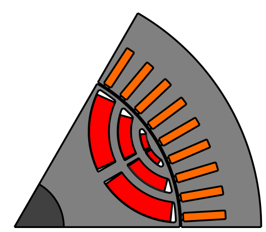

(b)

Fig. 7. Designed machine cross sections: (a) PMSM and (b) PM-SyR motor

different characteristic currents. It must be remarked that the PM-SyR motor was selected with this margins also to cope with the demagnetization limit, that is another big issue of ferrite PMs. In facts, the IPM motor with NdFeB PMs is safe against demagnetization also in short-circuit, while the ferrite PM-SyR motor demagnetize if short-circuit happens.

## V. Conclusion

In this paper, two PMSMs motors for traction application are designed and compared, one using NdFeB PMs and one with ferrite PMs. The $(x, b)$ design plane implemented in the open-source environment SyR-e is adopted and new performance figures as the short-circuit current and PM demagnetization index are introduced. Furthermore, the strategies

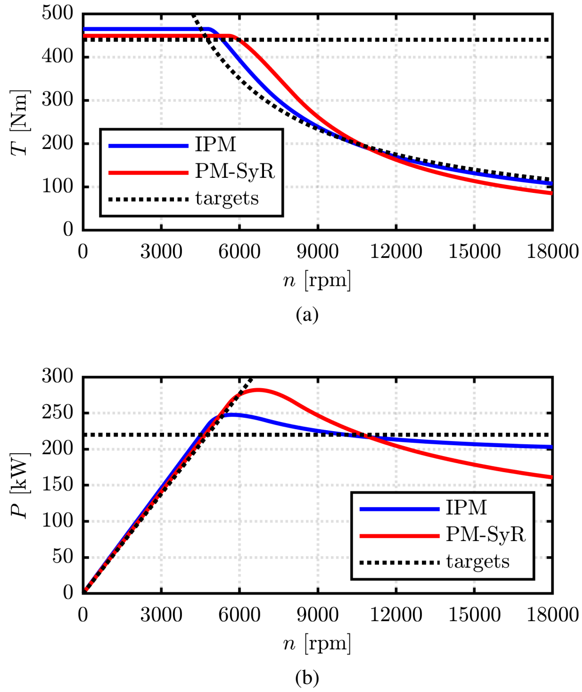


Fig. 8. Operating curves of the two motors at maximum inverter limits: (a) torque and (b) power.

TABLE II
DESIGNED MOTOR SPECIFICATIONS COMPARISON.

| | | IPM | PM-SyR | |
|---|---|---|---|---|
| | $x$ | 0.66 | 0.67 | |
| | $b$ | 0.57 | 0.64 | |
| Stator outer diameter | $D$ | 225 | 225 | [mm] |
| Stack length | $L$ | 114 | 211 | [mm] |
| Peak torque | $T$ | 444 | 437 | [Nm] |
| Power factor | $cos\varphi$ | 0.74 | 0.62 | |
| Peak power | $P$ | 225 | 256 | [kW] |
| Base speed | $n_{base}$ | 4845 | 5593 | [rpm] |
| DC link voltage | $V_{dc}$ | 320 | 320 | [V] |
| Peak phase current | $I_{max}$ | 1131 | 1556 | [Apk] |
| Number of turns | $N_s$ | 18 | 9 | |
| Characteristic current | $I_{ch}$ | 632 | 357 | [Apk] |
| HWC current | $I_{HWC}$ | 2329 | 3273 | [Apk] |
| Demag vol @ $I$ | $dPM_0$ | 0% | 0% | [pu] |
| Demag vol @ $I_{HWC}$ | $dPM_{HWC}$ | 0% | 100% | [pu] |

to optimize the design and understand all the information included in the $(x, b)$ plane are reviewed and explained thanks to the two case studies. The results of the comparison highlight that the ferrite PM-SyR offers a rare-earth-free design at the cost of a 47% longer stack and a higher inverter current (+37.5%). Furthermore, demagnetization is very critical for the PM-SyR machine, with 100% of the PM volume irreversibly demagnetized if a short-circuit happens, although an active short circuit is unnecessary for this type of motor due to the non-dangerous open-circuit EMF magnitude. The presented new features are included in the public version of SyR-e.

## ACKNOWLEDGMENT

The research has been conducted with the support of Power Electronics Innovation Center (PEIC) of Politecnico di Torino.

## REFERENCES

[1] A. Krings and C. Monissen, “Review and Trends in Electric Traction Motors for Battery Electric and Hybrid Vehicles,” in *2020 International Conference on Electrical Machines (ICEM)*, vol. 1, Aug. 2020.
[2] C. S. Goli, M. Manjrekar, S. Essakiappan, P. Sahu, and N. Shah, “Landscaping and Review of Traction Motors for Electric Vehicle Applications,” in *2021 IEEE Transportation Electrification Conference & Expo (ITEC)*, Jun. 2021, pp. 162–168, iSSN: 2377-5483.
[3] P. Ragazzo, S. Ferrari, G. Dilevrano, L. Beatrici, C. Girardi, and G. Pellegrino, “Synchronous Reluctance Machines with and without Ferrite Assistance for Lifting Systems,” in *International Electric Machines and Drives Conference (IEMDC 2023)*, 2023.
[4] T. Jahns, “Getting Rare-Earth Magnets Out of EV Traction Machines: A review of the many approaches being pursued to minimize or eliminate rare-earth magnets from future EV drivetrains,” *IEEE Electrification Magazine*, vol. 5, no. 1, pp. 6–18, Mar. 2017.
[5] S. Jurkovic, K. Rahman, B. Bae, N. Patel, and P. Savagian, “Next generation chevy volt electric machines; design, optimization and control for performance and rare-earth mitigation,” in *2015 IEEE Energy Conversion Congress and Exposition (ECCE)*, Montreal, QC, Canada.
[6] P. Ragazzo, G. Dilevrano, S. Ferrari, and G. Pellegrino, “Design of IPM Synchronous Machines Using Fast-FEA Corrected Design Equations,” in *2022 International Conference on Electrical Machines (ICEM)*, Sep. 2022, pp. 1–7, iSSN: 2381-4802.
[7] G. Pellegrino and F. Cupertino, “SyR-e.” [Online]. Available: https://github.com/SyR-e
[8] Tesla, “Model 3 Owner’s Manual.” [Online]. Available: https://www.tesla.com/ownersmanual/model3/en_cn/GUID-E414862C-CFA1-4A0B-9548-BE21C32CAA58.html
[9] D. Meeker, “FEMM: Finite Element Method Magnetics.” [Online]. Available: www.femm.info
[10] S. Ferrari, P. Ragazzo, G. Dilevrano, and G. Pellegrino, “Flux and loss map based evaluation of the efficiency map of synchronous machines,” *IEEE Transactions on Industry Applications*, vol. 59, no. 2, pp. 1500–1509, 2023.
[11] A. Varatharajan, D. Brunelli, S. Ferrari, P. Pescetto, and G. Pellegrino, “syredrive: Automated sensorless control code generation for synchronous reluctance motor drives,” in *2021 IEEE Workshop on Electrical Machines Design, Control and Diagnosis (WEMDCD)*, 2021, pp. 192–197.
[12] Apache License - Version 2.0 January 2004. [Online]. Available: https://www.apache.org/licenses/LICENSE-2.0.txt
[13] S. Ferrari and G. Pellegrino, “FEAfix: FEA Refinement of Design Equations for Synchronous Reluctance Machines,” *IEEE Transactions on Industry Applications*, vol. 56, no. 1, pp. 256–266, Jan. 2020.
[14] S. Ferrari, P. Ragazzo, G. Dilevrano, and G. Pellegrino, “Determination of the Symmetric Short-Circuit Currents of Synchronous Permanent Magnet Machines Using Magnetostatic Flux Maps,” in *2021 IEEE Energy Conversion Congress and Exposition (ECCE)*, Oct. 2021, pp. 3697–3704, iSSN: 2329-3748.
[15] G. Dilevrano, P. Ragazzo, S. Ferrari, G. Pellegrino, and T. Burress, “Magnetic, Thermal and Structural Scaling of Synchronous Machines,” in *2022 IEEE Energy Conversion Congress and Exposition (ECCE)*, Oct. 2022, pp. 1–8, iSSN: 2329-3748.
[16] G. Berardi and N. Bianchi, “Design Guideline of an AC Hairpin Winding,” in *2018 XIII International Conference on Electrical Machines (ICEM)*, Sep. 2018, pp. 2444–2450, iSSN: 2381-4802.
[17] S. Xue, M. Michon, M. Popescu, and G. Volpe, “Optimisation of Hairpin Winding in Electric Traction Motor Applications,” in *2021 IEEE International Electric Machines Drives Conference (IEMDC)*, pp. 1–7.